Photocatalytic degradation of organic pollutants coupled with simultaneous photocatalytic H_2 evolution over graphene quantum dots/Mn-N-TiO_2/gC_3N_4 composite catalysts: Performance and mechanism

Yu-Chun Nie[a], Fan Yu[a], Lai-Chun Wang[a], Qiu-Ju Xing[a,*], Xia Liu[b], Yong Pei[b], Jian-Ping Zou[a,*], Wei-Li Dai[a], Yan Li[c], Steven L. Suib[d,*]

[a] Key Laboratory of Jiangxi Province for Persistent Pollutants Control and Resources Recycle, Nanchang Hangkong University, Nanchang, 330063, PR China [b] Key Laboratory of Environmentally Friendly Chemistry and Applications of Ministry of Education, Xiangtan University, Xiangtan, 411105, PR China [c] School of Chemistry & Molecular Engineering, East China University of Science and Technology, Shanghai, 200237, China [d] Department of Chemistry, University of Connecticut, Storrs, CT, United States

A B S T R A C T

Graphene quantum dots/Mn-N-TiO_2/g-C_3N_4 (GQDs/TCN) composite photocatalysts have been designed, synthesized and characterized by XRD, SEM, TEM, Raman, BET, and XPS. The photodegradation of organic pollutants (p-nitrophenol, diethyl phthalate and ciprofloxacin, called as 4-NP, CIP and DEP, respectively) coupled with simultaneous photocatalytic production of hydrogen was successfully achieved using the GQDs/TCN catalysts. The 5%GQDs/TCN-0.4 sample shows the best photocatalytic hydrogen production and organic pollutant degradation rate under simulated solar irradiation in the simultaneous photocatalytic oxidation and reduction system. Furthermore, the photocatalytic H_2 evolution rates in the solution of 4-NP, CIP and DEP are all larger than that in pure water system over the 5%GQDs/TCN-0.4 catalyst. And the H_2 evolution rate in the solution of 4-NP is smaller than that in the solutions of CIP and DEP. Accordingly, the photodegradation rate of 4-NP is larger than that of CIP and DEP. The analyses of density functional theory and liquid chromatography mass spectrometry indicate that some photogenerated electrons were used in the photodegradation process of 4-NP but not in that of CIP and DEP. And it leads to the photocatalytic rate of H_2 evolution in the 4-NP solution smaller than that in the solution of CIP and DEP. For the first time, the present work illuminates the photocatalytic enhancement of the GQDs/TCN-0.4 catalyst and the mechanism of the effect of different organic pollutants on photocatalytic H_2 evolution.

1. Introduction

In recent years, the energy crisis and environment pollution have been the main aspects of environmental problems, among which water pollution has especially aroused much attention [1,2]. Generally, water pollution is mainly caused by contaminants of heavy-metal ions and organic pollutants, such as hormones, dyes, aromatics, pesticides, and perfluorinated organic compounds (PFOCs). Among them, the organic pollutants in wastewater exhibit high toxicity, carcinogenicity and refractory degradation, which poses a great threat to human health [3–7]. Therefore, it is very urgent to developing efficient technologies for removal of organic pollutants from water.

Photocatalysis, as a green and sustainable technology, has attracted considerable interest due to being able to simultaneously tackle the energy crisis and environmental contamination by using solar energy [8–11]. Photocatalysis technologies consist of photocatalytic oxidation and photocatalytic reduction. In the oxidation process, solar energy was converted into actively free radicals over catalysts to oxidize organic pollutants to CO_2 and H_2O [12]. For the reduction process, solar energy was converted to photogenerated electrons that can result in H_2 evolution from water splitting or CO_2 reduction to useful hydrocarbons (such as methane, ethanol, methanol and so on) using catalysts [13]. In theory, if we could combine photocatalytic oxidation with photocatalytic reduction in a photocatalytic system, the quantum efficiency and the separation efficiency of photo-generated holes and electrons would be markedly improved, which would result in excellent degradation of organic pollutants and good energy utilization. Until now, our group has developed a composite catalyst with good photocatalytic performance of degradation of organic pollutants coupled with simultaneous CO_2 reduction [14,15], demonstrating the combination of photocatalytic oxidation and photocatalytic reduction can be fulfilled in a catalytic system.

However, until now, there are only a few reports on the combination of the degradation of organic pollutants with hydrogen evolution in a photocatalytic system [16,17]. These studies did not investigate the influence of different types of organic pollutants on photocatalytic hydrogen production [18]. And the literature just reported bifunctional photocatalysts for degradation of organic pollutants and photocatalytic hydrogen evolution [19]. Therefore, it is very important to develop a photocatalytic system to realize the degradation of organic pollutants with simultaneous photocatalytic H_2 evolution and make clear the synergistic mechanism of photocatalytic oxidation and photocatalytic reduction.

Titanium dioxide (TiO_2) photocatalysis has attracted wide attention because the valence band (VB) is more positive than the oxidation potentials of many organic pollutants, leading to good photodegradation of organic pollutants [20–24]. However, due to the drawbacks of a wide band gap (3.2 eV) and high recombination rate of photogenerated holes and electrons, the photocatalytic performance of titania is seriously restricted. Metal and nonmetal co-doping was considered as a good method to improve the visible light absorption and photocatalytic activity of TiO_2 [25–30]. The nitrogen-doped TiO_2 (TiO_2-N) has been investigated [31–33], demonstrating that the N modification can enhance the visible light absorption of TiO_2. And some literatures reported that TiO_2 with the manganese modification can effectively improve the photocatalytic performance of TiO_2 [34,35]. Therefore, Mn and N co-doping would combine the advantage of Mn and N modification and then markedly improve the photocatalytic activity of TiO_2. In addition, graphitic carbon nitride (g-C_3N_4) has been extensively investigated for potential applications in photocatalytic H_2 evolution from water splitting because the minimum of the conduction band (CB) is more negative than the potential of the normal hydrogen electrode (NHE) [36]. However, the photocatalytic performance of g-C_3N_4 still has some defects [37,38]. For example, the photocatalytic performance of g-C_3N_4 is still restricted by the high recombination rate of photogenerated electron-hole pairs, low specific surface area, and limited active sites [39].

Therefore, in order to develop a new photocatalytic system to fulfill simultaneous photodegradation of organic pollutants and photocatalytic hydrogen generation, we combined g-C_3N_4 with Mn-N-TiO_2 to prepare a novel heterostructured photocatalyst that can make full use of the synergistic effect of photocatalytic oxidation (photodegradation of organic pollutants) and photocatalytic reduction (photocatalytic H_2 generation). Furthermore, graphene quantum dots (GQDs) are graphene fragments that have more "molecule-like" character. GQDs display some competitive properties, such as high electrical/thermal conductivity, up-conversion of fluorescence, quantum confinement, and high surface area [40]. Specifically, GQDs can be used to modify semiconductor photocatalysts to enhance the photocatalytic performance of catalysts.

Given all the above, we combined GQDs with g-C_3N_4 and Mn-NTiO_2 to prepare GQDs/Mn-N-TiO_2/g-C_3N_4 composite photocatalysts by hydrothermal reaction methods. Herein, we report the design of a photocatalytic system to realize simultaneous photodegradation of organic pollutants and photocatalytic H_2 generation from water splitting by using the GQDs/Mn-N-TiO_2/g-C_3N_4 composite catalyst. And the synergistic photocatalytic mechanism was investigated to explain the effects of different organic pollutants on the rate of photocatalytic H_2 production. The present work not only provides an ideal scenario of the combination of photodegradation and photoreduction, but also opens a new avenue to achieve the removal of organic pollutants from wastewater coupled with the simultaneous generation of new energy.

2. Experimental section

2.1. Materials and measurement

The samples were characterized by X-ray diffraction (XRD) for phase identification on a Bruker D8 ADVANCE diffractometer with CuKα (λ = 1.5406 Å) radiation. Raman spectra were recorded on a microscopic confocal Raman spectrometer (JY LabRam HR800) with a laser source of 785 nm. Morphology and structure were studied with a field emission scanning electron microscope (SEM, Sirion 200, FEI, Holland) and a transmission electron microscope (TEM, Tecnai F20, FEI, USA), as well as a high-resolution transmission electron microscope (HRTEM). The chemical compositions and elemental mappings of the samples were determined by energy-dispersive X-ray spectrometer (EDX) equipped on SEM. Ultraviolet-visible (UV–vis) diffuse reflection spectra were measured using a UV–vis U-3900H spectrophotometer. Composition analyses on several randomly selected samples of the asprepared catalysts were performed on a field emission scanning electron microscope equipped with an energy dispersive X-ray instrument (EDX). Brunauer-Emmett-Teller (BET) surface area measurements were performed with a Micromeritics surface area analyzer at 77 K by using an adsorption apparatus. X-ray photoelectron spectroscopy (XPS) was obtained by using a VG 250 Escalab spectrometer equipped with an Al anode (Al-Kα = 1486.7 eV) as an X-ray source.

Electrochemical measurements were performed on a CHI 660D electrochemical workstation (Shanghai Chenhua, China), in the standard three-electrode cell system. There were platinum electrodes as counter electrode and standard calomel reference electrode in saturated KCl. The working electrodes were prepared by dip-coating: 10 mg of photocatalyst by supersonic extraction in 5 mL deionized water to produce a stable suspension that was then dip-coated onto a 4 cm × 1 cm fluorine-tin oxide (FTO) glass electrode, and the films were dried at room temperature. The electrolyte solution was Na_2SO_4 (0.5 M). As for photocurrent measurements, a 300 W Xe lamp was used as the source of simulated solar irradiation and the other conditions were the same as those of electrochemical measurements.

2.2. Syntheses

2.2.1. Synthesis of Mn-N- TiO_2 microspheres

The manganese and nitrogen co-doped mesoporous TiO_2 was synthesized via a modified hydrothermal reaction process [36]. Typical experimental procedures are shown below. First, a calculated amount of $Mn(C_2H_3O_2)_2{\cdot}4H_2O$ and 1.98 g of hexadecylamine (HDA) was dropwise added into a mixture of ethanol (200 mL) and potassium chloride solution (1.6 mL) to obtain a turbid solution under magnetic stirring. After stirring for 20 min, 1.5 mL titanium isopropoxide (TIP) was dropwise added to the above turbid solution under vigorous stirring. Then, the resultant light gray precipitate was obtained and dried at 160 °C for 16 h after aging at room temperature for 12 h, and then calcined at 500 °C for 2 h. Then the sample of (0.2at%)Mn-TiO_2, was obtained. Second, 0.2 g of the as-prepared (0.2at%)Mn-TiO_2 and 0.1 mL of ammonia solution (0.26 mol/L) were dispersed into a 20 mL mixture of ethanol and water. Then the above solution was transferred into a Teflon-lined stainless-steel autoclave at 180 °C for 2 h. Finally, a gray power of (0.2at%)Mn-(2at%)N-TiO_2 was obtained after calcination at 500 °C for 2 h.

2.2.2. Synthesis of g-C_3N_4 nanosheets

First, the bulk g-C_3N_4 was prepared by thermal polycondensation. Typically, 5 g melamine powder was put into an alumina crucible with a cover and kept at 550 °C for 4 h. Then the resulting yellow product of bulk g-C_3N_4 (CNB) was collected and ground into powder for further use. Second, 1 g of as-prepared CNB was added into the alumina crucible and heated at 793 K for 2 h. Finally, a faint yellow powder of gC_3N_4 nanosheets (CNS) was obtained.

2.2.3. Synthesis GQDs/TCN-0.4 nanocomposites

GQDs were synthesized by the reported method [41]. The as-prepared Mn-N-TiO_2 (0.1 g) was physically mixed with a given amount of CNS, and then maintained at 400 °C in an alumina crucible (heating ramp is 2 °C min^{-1}) for 60 min. Mn-N-TiO_2/CNS composites (called

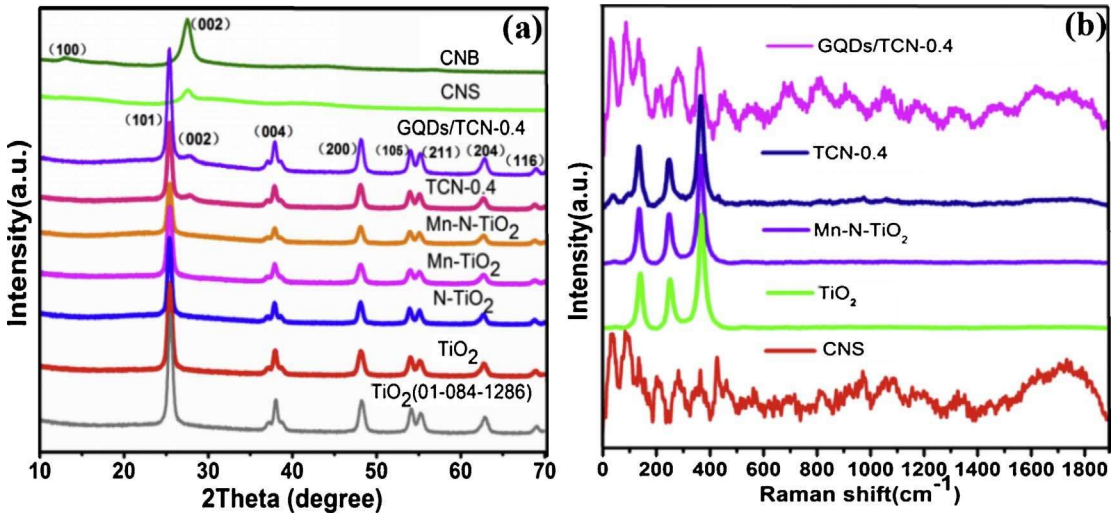

Fig. 1. XRD patterns of the as-prepared TiO_2, CNB, CNS, Mn-TiO_2, N-TiO_2, Mn-N-TiO_2, TCN-0.4, and GQDs/TCN-0.4 (a); and Raman spectra of TiO_2, CNS, Mn-N-TiO_2, TCN-0.4, and GQDs/TCN-0.4 (b).

TCN) were obtained. The weight ratio of CNS against Mn-N-TiO_2 was controlled to be 10, 20, 30, 40 and 50 (wt%), respectively. The resulting samples were labeled as TCN-x, where x equal to 0.1, 0.2, 0.3, 0.4, and 0.5. In addition, 0.103 g of the as-prepared TCN-0.4 sample and 2.5 mL GQDs (0.205 mg/mL) were dispersed into 10 mL deionized water, and then the aqueous solution was vigorously stirred for 24 h. Finally, the composites of GQDs/TCN-0.4 with different amounts of gC_3N_4 nanosheets were obtained by centrifugation and desiccation at 80 °C for 3 h.

2.3. Test of photocatalytic activity

The photocatalytic activities of as-prepared samples were evaluated by the degradation of typical organic pollutants (p-nitrophenol, ciprofloxacin and diethyl phthalate) under simulated solar irradiation. A 300 W Xe lamp (Wavelength range: 320 nm ≤λ≤ 780 nm, light intensity: 160 mW/cm^2) was used as the source of light. The solid catalyst (45 mg) was dispersed in an 80 mL solution containing organic pollutant (10 ppm 4-NP, CIP or DEP). Then 3 wt% Pt was loaded onto the sample surfaces by photodeposition of H_2PtCl_6. An aqueous solution was added into a Pyrex top-irradiation reaction vessel connected to a glass-closed gas system (Prefect Light, Beijing, Labsolar-III (AG), see Fig. S1 in Supporting Information). The whole reaction setup was evacuated by using a vacuum pump to completely remove air. High purity argon gas was used as a carrier gas. Before irradiation, the solution was stirred in the dark for 1 h to reach an adsorption-desorption equilibrium, and the amount of hydrogen evolution from photocatalytic splitting water was analyzed by using an online gas chromatograph with a thermal conductivity detector (TCD) and a capillary column (5 Å molecular sieve). The temperature of the reaction solution was maintained at 6 °C by an external flow of cold water (constant temperature device XODC-0506, Nanjing Shunliu, China). During specific time intervals, fixed amounts of the reactant solution were extracted and filtered. The photocatalytic degradation rate was tested via the intensity changes of the absorption peak at 401 nm (under alkaline medium) to determine the concentration of 4-NP with a UV–vis spectrophotometer (UV-2550, Shimadzu, Japan), whereas the concentrations of DEP and CIP were quantified with an HPLC (SHIMADZU (Japan)) with an XBC18 column (10 cm × 4.6 mm, 2.7 m) at 224 nm and 277 nm, respectively. The mobile phase consisted of two solvents: 80% methanol and 20% DI water were used for DEP; 20% A (acetonitrile) and 80% B (0.1% formic acid) were used for CIP. The intermediates were detected with an LC-MS (Thermo, Finnigan, LCQ-Deca xp) equipped with an electrospray ionization (EIS) source. The samples were injected at a flow rate of 0.2 mL/min under isocratic conditions. The ion mode was set on positive mode and the mobile phase was methanol-water (0.1% formic acid) (60:40, v/v). A 2 uL extract was injected using the auto sampler.

2.4. Density functional theory (DFT)

All the calculations based on density functional theory (DFT) were performed with a DMol3 package with a Perdew-Burke-Ernzerhof/ Double-Numerical Dasis 4.4 set. All computations converged upon a true energy minimum, which was confirmed by the absence of imaginary frequencies. The cutoff radius was 4 Å. Based on the Frontier Orbital Theory, the electrophilic reaction most likely takes place at atoms with high values of the highest occupied molecular orbital (HOMO), whereas the nucleophilic reaction most likely occurs at the atoms with high values of the lowest unoccupied molecular orbital (LUMO) [42]. Thus the FEDs (Frontier electron densities) of the HOMO and LUMO of compounds were calculated [43].

3. Results and discussion

3.1. Characterizations

XRD patterns of TiO_2, CNB, CNS, Mn-TiO_2, Mn-N-TiO_2, TCN-0.4, GQDs/TCN-0.4 are shown in Fig. 1a. For the CNB, the strong (0 0 2) peak at 27.3° and the (1 0 0) peak at 13.1° correspond to the inter-layer and in-plane crystal facets of g-C_3N_4, respectively. Compared with CNB, the peak intensities of CNS at 27.3° and 13.1° markedly decreased, indicating that the CNB has been successfully exfoliated into nanosheets. The diffraction patterns of the as-prepared Mn-TiO_2, N-TiO_2 and Mn-NTiO_2 are well matched with that of the anatase TiO_2 (JCPDS 01-0841286), showing that the doping of Mn and N in TiO_2 does not introduce impurity phases and does not cause any obvious change in TiO_2 crystallinity. Compared with the (1 0 1) peak of TiO_2, the (1 0 1) peak of Mn-N-TiO_2 has a shift toward slightly lower angle (Fig. S2 in SI), suggesting that the Ti^{4+} in TiO_2 was partially substituted by Mn^{2+} and N^{3-} because the ionic sizes of Mn^{2+} (0.08 nm) and N^{3-} (0.146 nm) are both larger than that of Ti^{4+} (0.0605 nm) [44]. For the TCN-0.4 and GQDs/TCN-0.4, all of the diffraction peaks correspond to those of gC_3N_4 and Mn-N-TiO_2. There are no diffraction peaks of GQDs observed in the GQDs/TCN-0.4 composite, which could be due to the low content and relatively low diffraction intensity of GQDs.

As shown in Fig. 1b, the Raman peaks of Mn-N-TiO_2, TCN-0.4 and GQDs/TCN-0.4 show the characteristic peaks of typical anatase TiO_2 (143, 395, 515, and 636 cm^{-1}) [45]. The GQDs/TCN-0.4 shows two typical D and G bands of GQDs (Fig. S3 in SI), assigned to sp^3 defects and in-plane vibration of sp^2 carbon in graphene, respectively, confirming the existence of GQDs [46].

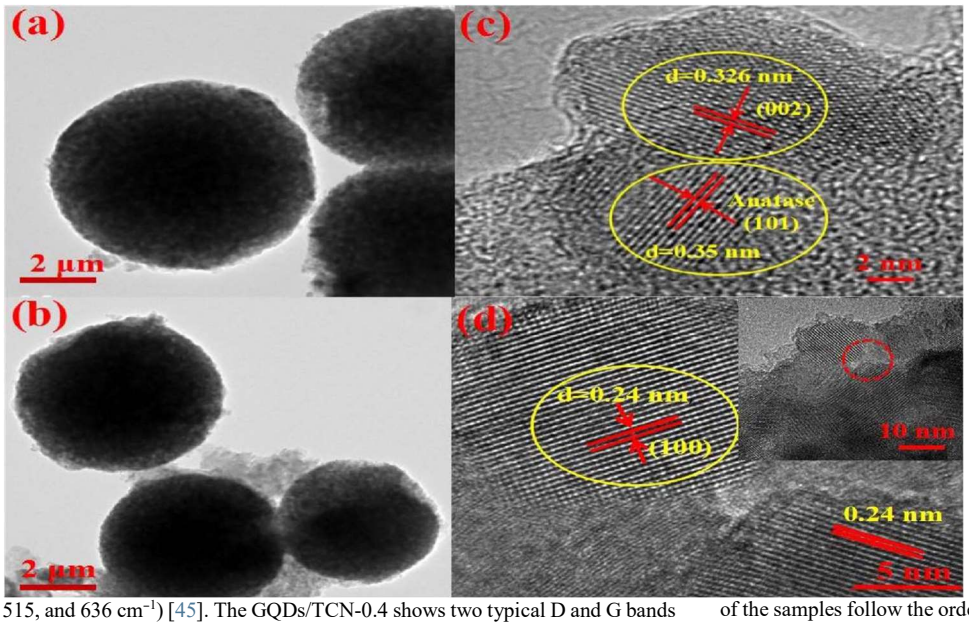

Fig. 2. TEM images of Mn-N-TiO_2 (a) and GQDs/ TCN-0.4 (b); HRTEM images of TCN-0.4 (c) and GQDs/TCN-0.4 (d).

Fig. S4a shows that Mn-N-TiO_2 exhibits microspheres with diameters of approximately 0.5–1 μm, and the thin-layered CNS coupled with the microspheres of Mn-N-TiO_2 (Fig. S4b). Fig. 2a shows that the microspheres of Mn-N-TiO_2 are composed of a large number of nanoparticles, whereas the thin-layered CNS is deposited on the surface of Mn-N-TiO_2 among the GQDs/TCN-0.4 (Fig. 2b). In addition, HRTEM images of the GQDs/TCN-0.4 show that GQDs are well dispersed on the surface of TCN-0.4 with diameters of ≈10 nm. The lattice spacing distances of 0.35, 0.326 and 0.24 nm correspond to the (1 0 1) planes of the anatase phase of TiO_2 and the (0 0 2) of the g-C_3N_4 and the (1 0 0) facet of graphene (Fig. 2c and d), respectively [46,47]. EDS analysis confirms the existence of Ti, O, N, and Mn (Fig. S5 in SI). And the calculated content of Mn and N in the Mn-N-TiO_2 is 0.80 at% and 0.11 at%, respectively, which approaches to the denoted content in our experiment. The above results indicate that GQDs were successfully attached to the surfaces of the TCN-0.4.

BET surface areas of the as-prepared CNB, CNS, Mn-N-TiO_2, TCN-0.4, and GQDs/TCN-0.4 are calculated as 6.02, 149.6, 45.5, 50.25, and 52.25 m^2/g, respectively (Fig. S6 in SI). The CNS shows a larger surface area than the CNB, confirming that nanosheets of g-C_3N_4 plausibly have been successfully obtained from the exfoliation of CNB.

As described in Fig. S7a, TCN-0.4 has an absorption onset at 480 nm and shows a marked red-shift compared with TiO_2, CNS and Mn-N-TiO_2. The energy gaps (Eg) of CNS and Mn-N-TiO_2 are calculated to be 2.80 and 2.90 eV, respectively (Fig. S7b). When GQDs were loaded on TCN-0.4, the light absorption of GQDs/TCN-0.4 shows a great increase in the visible light region. The peak intensity of the PL spectra of TiO_2, Mn-N-TiO_2, TCN-0.4, and GQDs/TCN-0.4 successively decreased (Fig. 3a), indicating that the composite of GQDs/TCN-0.4 shows the worst electron and hole recombination rate. Furthermore, Fig. 3b shows the upconversion property of GQDs. When GQDs was excited by long wavelengths from 600 to 800 nm, this generates emissions located in the range of 450–500 nm. This upconversion PL property of GQDs could be attributed to multiphoton active processes similar to previous reports [48]. Transient photocurrent response measurements are shown in Fig. 3c. The photocurrent intensities of the as-prepared samples show the order of TiO_2 < Mn-NTiO_2 < TCN-0.4 < GQDs/TCN-0.4, indicating that GQDs/TCN-0.4 has the best separation rate of photo-generated electrons and holes.

Electrochemical impedance spectra (EIS) were recorded to investigate the electrochemical properties of the samples. As shown in Fig. 3d, the resistances of the samples follow the order of TiO_2 > Mn-NTiO_2 > TCN-0.4 > GQDs/TCN-0.4, suggesting that GQDs/TCN-0.4 can more efficiently promote the separation and transfer of photogenerated electrons and holes than TiO_2, Mn-N-TiO_2 and TCN-0.4. The above results confirm that the introduction of GQDs and CNS, as well as the co-doping of Mn and N can effectively separate photo-generated electrons and holes and promote light absorption, and further improve the photocatalytic performance of TiO_2.

As shown in Fig. 4a, two peaks were observed at 458.5 and 464.1 eV among the Ti 2p spectra of Mn-N-TiO_2 and GQDs/TCN-0.4 that are ascribed to Ti $2p^{3/2}$ and Ti $2p^{1/2}$, respectively [45]. Fig. 4b demonstrates that the O 1 s peaks around 529.8 and 531.3 eV are assigned to the Ti-O bonds in the TiO_2 lattice and the hydroxyl groups or water adsorption on TiO_2 surfaces, respectively. The high resolution C 1 s spectra of GQDs/TCN-0.4 show four peaks at 284.6, 285.3, 288.0, and 289.2 eV (Fig. 4c). The peak at 284.6 eV corresponds to sp^2 CeC bonds of graphitic carbon nitride and GQDs, whereas those at 285.3 eV, 288.0 eV and 289.2 eV are attributed to CeOH bonds, CeNeC bonds and NeC]N configurations, respectively [49,50]. As shown in Fig. 4c, compared with the TCN-0.4, the intensities of the peaks at 284.6 eV and 285.3 eV among the GQDs/TCN-0.4 composite are obviously enhanced, indicating that GQDs were successfully loaded on the TCN-0.4.

As shown in Fig. 4d, the main signal of N 1 s spectra showed the occurrence of CeNeC groups (398.1 eV) and NeTieO groups (399.9 eV) [48,49]. From Fig. 4e, two peaks at 641.4 and 653.4 eV are ascribed to the Mn $2p^{3/2}$ and Mn $2p^{1/2}$ transitions for Mn species on the surface of Mn-N-TiO_2, respectively, indicating that the valence state of Mn in the GQDs/TCN-0.4 is +2. After photocatalytic reaction for 2 h, the peak positions at 641.4 and 653.4 eV did not change (Fig. 4e), showing the valence of Mn is unchanged during the photocatalytic process and Mn did not participate in the reaction [44,45]. The results of XPS confirm that the successful co-dopants of Mn and N exist in TiO_2 and so does the existence of GQDs and CNS in the GQDs/ TCN-0.4. Meanwhile, according to the result of XPS, the calculated content of Mn and N in the Mn-N-TiO_2 is 0.21 at% and 2 at%, respectively, which approaches to the denoted content in our experiment. Furthermore, on the basis of the above XRD, Raman, BET, SEM, TEM, and XPS results, GQDs/TCN-0.4 composites have been successfully fabricated.

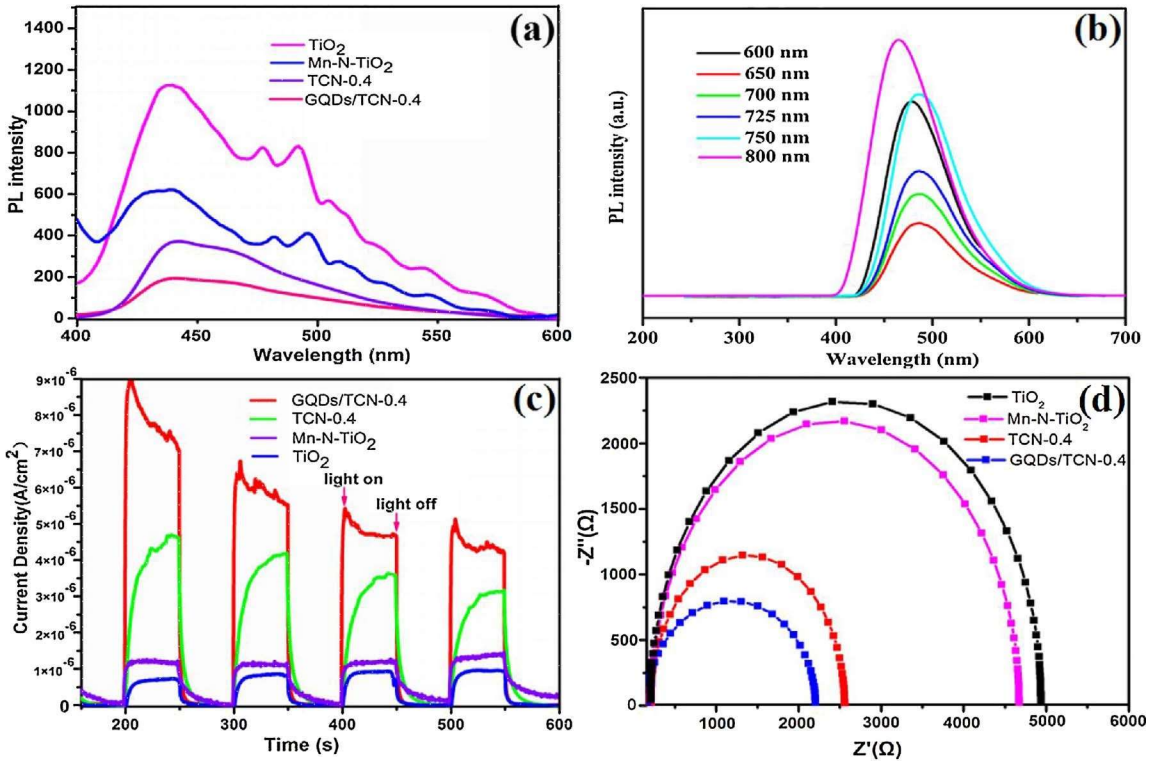

Fig. 3. PL spectra of the as-prepared TiO_2, Mn-N-TiO_2, TCN-0.4, and GQDs/TCN-0.4 (a); and upconversion PL properties of GQDs excited by long wavelength from 600 to 800 nm (b); photocurrent transient responses of the as-prepared samples (c); Electrochemical impedance spectra of the as-prepared catalysts (d).

3.2. Photocatalytic activity

Photocatalytic H_2 evolution activity of the as-prepared catalysts was evaluated under simulated solar irradiation in solution containing different organic pollutants (4-NP, CIP or DEP) for 2 h. Fig. 5a shows the photocatalytic activities of the combination of degradation of 4-NP with hydrogen evolution over the GQDs/TCN-x with different amounts of CNS. With the increase of loading amount of CNS, the photodegradation rate of 4-NP and H_2 evolution rate increase, but the H_2 evolution rate decreases and photodegradation rate of 4-NP nearly remains the same when the loading amount of CNS is larger than 40 wt%. The 5%GQDs/ TCN-0.4 shows the highest photocatalytic activities with an 89% removal rate of 4-NP and a H_2 evolution rate of 0.87 mmol L^{-1} g^{-1} after 2 h photocatalytic reaction. The results indicate that a suitable loading amount of CNS is the key to the photocatalytic performance of GQDs/ TCN-0.4 because this would lead to excellent efficiency of light absorption and a desirable separation rate of photogenerated electrons and holes.

In addition, the photocatalytic activities of GQDs, CNS, and the physical mixture of 5%GQDs and TCN-0.4 were investigated. As shown in Fig. 5b, the photocatalytic degradation rate of 4-NP is only 13.4% and 11.8% over the GQDs/Mn-N-TiO_2 and Mn-N-TiO_2, respectively, and the H_2 evolution rates is 0.512 mmol L^{-1} g^{-1} and
0.441 mmol L^{-1} g^{-1}, respectively. The low photocatalytic activity of the GQDs/Mn-N-TiO_2 and Mn-N-TiO_2 could be due to their fast recombination rate of photogenerated holes and electrons. The photocatalytic degradation rate of 4-NP and H_2 evolution rate over TCN-0.4 are 80% and 0.82 mmol L^{-1} g^{-1}, respectively, after 2 h photocatalytic reaction, while 5%GQDs/TCN-0.4 shows a 4-NP removal rate of 89% and H_2 evolution rate of 0.87 mmol L^{-1} g^{-1}, indicating that GQDs can enhance the photocatalytic activity of the sample. The physical mixture of 5%GQDs, 40%CNS and Mn-N-TiO_2 exhibits a 4-NP removal rate of 45% and a H_2 evolution rate of 0.47 mmol L^{-1} g^{-1}, respectively, much lower than 5%GQDs/TCN-0.4 (Fig. 5b), which confirms the formation of good contacts between GQDs, CNS, and Mn-N-TiO_2 in the 5%GQDs/ TCN-0.4 composite.

Furthermore, in order to illuminate the relationship of photocatalytic hydrogen evolution and the removal of different organic pollutants, the photocatalytic H_2 production in different solutions containing different organic pollutants was investigated by using the 5%GQDs/TCN-0.4 under simulated solar irradiation. As shown in Fig. 6a, the photocatalytic H_2 production rate follows the order of CIP > DEP > 4-NP > H_2O, showing that the photocatalytic H_2 evolution rate increases with the addition of CIP, DEP or 4-NP in the photocatalytic system. Accordingly, the degradation rates of CIP, DEP and 4-NP are 89%, 70.4%, and 48.6%, respectively, over the 5%GQDs/ TCN-0.4. The results show that the photocatalytic H_2 production and simultaneous photodegradation of organic pollutants can be achieved via the 5%GQDs/TCN-0.4 composite catalyst, and the photocatalytic H_2 evolution rate is affected by the different organic pollutants. Fig. S8a shows that the concentration of 4-NP markedly decreases with reaction time according to time-dependent UV–vis absorption spectra of 4-NP. Figs. S8b and S8c show the intensities of the corresponding characteristic peaks significantly decrease with reaction time based on the characteristic chromatograms of DEP and CIP. The results imply that 4NP, DEP, and CIP can be efficiently degraded by the 5%GQDs/TCN-0.4 composite catalyst.

In addition, the effect of different initial concentrations of pollutants on H_2 production was researched in the closed gas system by 5%GQDs/ TCN-0.4. As shown in Fig. 6b, the production rate of hydrogen decreases with an increase of initial concentration of 4-NP, whereas the removal amount of 4-NP increases with an increase of initial concentration of 4-NP. The result could be explained that more 4-NP molecules on the surface of catalyst would be degraded in 4-NP solution with higher initial concentration, and more generated intermediates in 4-NP solution with higher initial concentration would consume photogenerated electrons and then lead to a lower photocatalytic H_2 production rate. Further research on the stability of the 5%GQDs/TCN-0.4 was investigated by a five-run cycling test in the closed gas system. As shown in Fig. 6c, there is just a little decrease for the degradation rate of

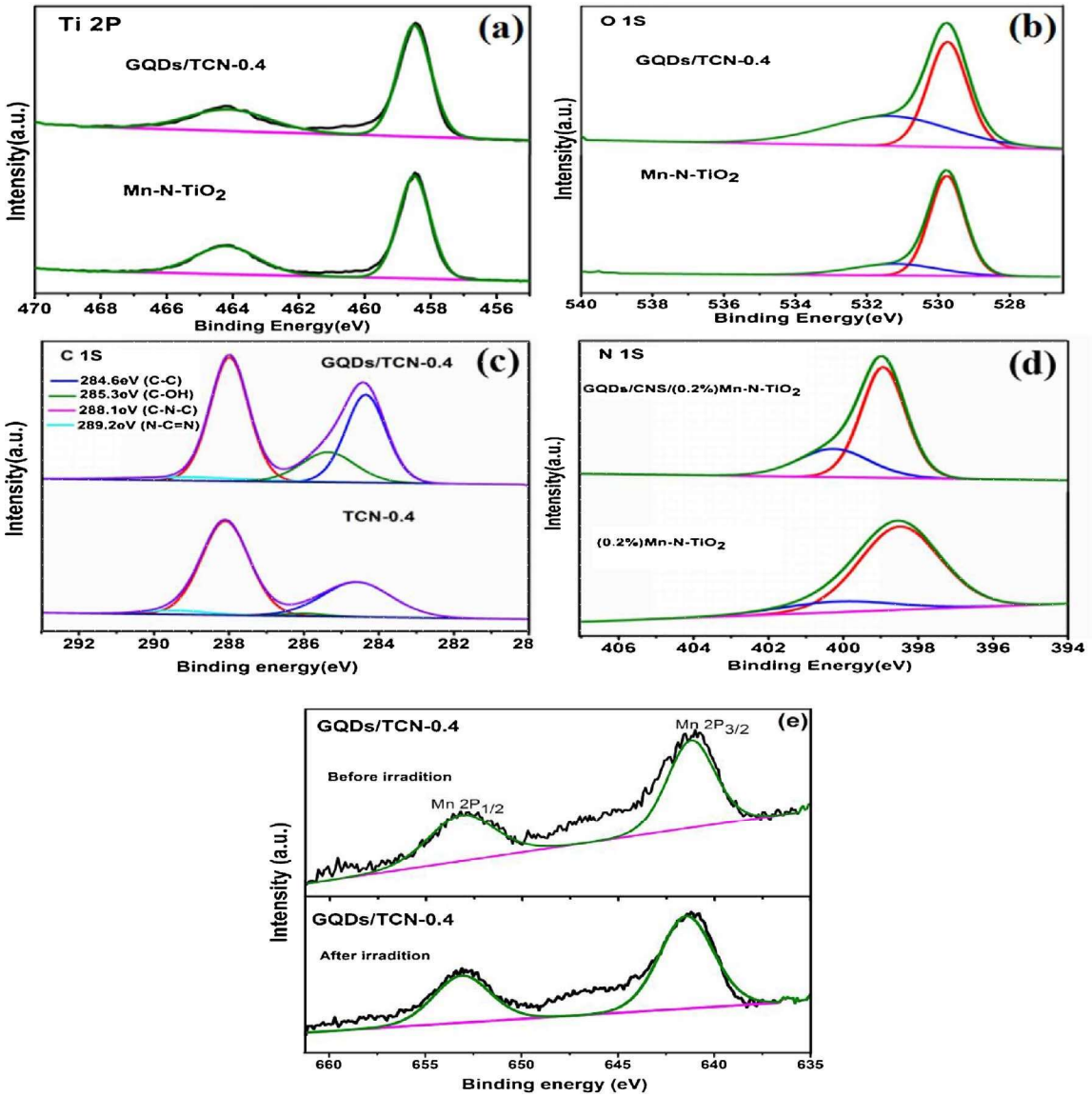

Fig. 4. XPS spectra for Ti 2p of Mn-N-TiO_2 and 5%GQDs/TCN-0.4 (a); O 1s of Mn-N-TiO_2 and 5%GQDs/TCN-0.4 (b); C 1 s of TCN-0.4 and 5%GQDs/TCN-0.4 (c); N 1 s of Mn-N-TiO_2 and 5%GQDs/TCN-0.4 (d); and Mn 2p of 5%GQDs/TCN-0.4 before and after photocatalytic reaction for 2h (e).

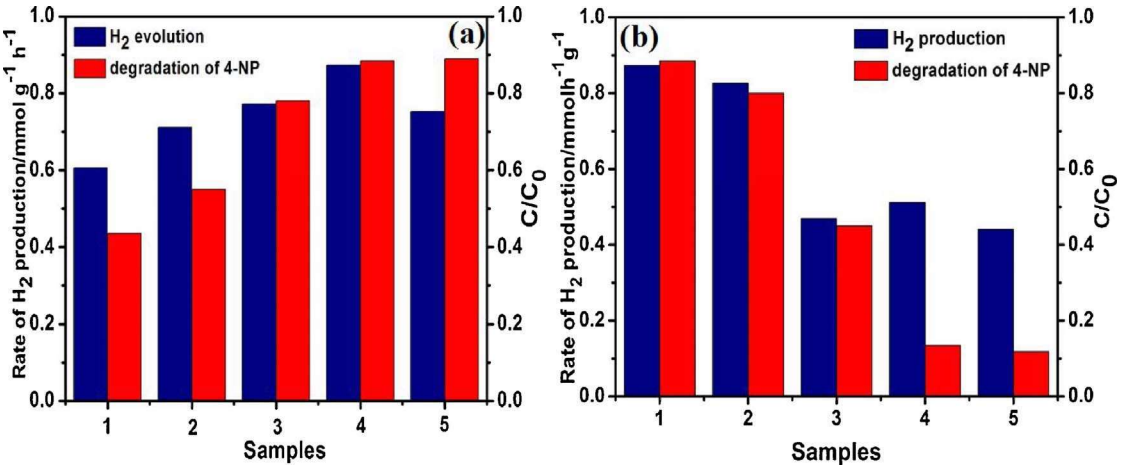

Fig. 5. The combination of degradation of 4-NP with hydrogen evolution under simulated solar irradiation over the as-prepared GQDs/TCN-x composites with different loadings of CNS (1: 10%, 2: 20%, 3: 30%, 4: 40%, 5: 50%) (a); and the photocatalytic process over the as-prepared samples (1: GQDs/TCN-0.4; 2: TCN-0.4; 3: physical mixture of GQDs, Mn-N-TiO_2 and CNS; 4: GQDs/Mn-N-TiO_2; 5: Mn-N-TiO_2) (b).

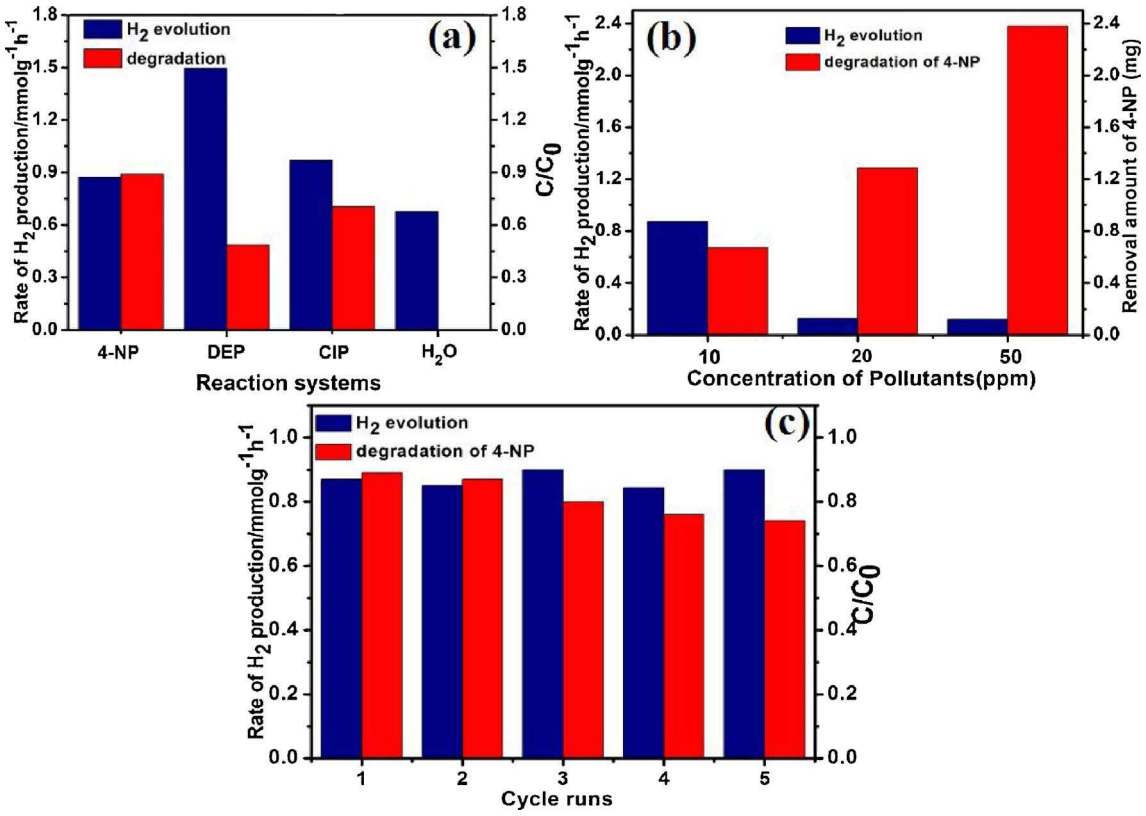

Fig. 6. Simultaneous photodegradation of organic pollutants coupled with hydrogen evolution by using 5%GQDs/TCN-0.4 at different reaction systems (a) and at different initial concentration of pollutant 4-NP (b); cycling test in the closed gas system over the 5%GQDs/TCN-0.4 under simulated solar irradiation (c).

4-NP after 10 h (five runs), and the H_2 evolution rate is almost unchanged. The result confirms that 5%GQDs/TCN-0.4 has high stability.

3.3. Photocatalytic mechanism

In order to investigate reactive species generated in the degradation process, trapping experiments were carried out. Since the photocatalysis experiment was carried out in a closed glass gas system in a vacuum system, we only considered hydroxyl radicals (%OH), electron (e^-), and holes (h^+) by adding 1.0 mM tert-butyl alcohol (t-BuOH), potassium persulfate ($K_2S_2O_8$) and ethylenediaminetetraacetic acid (EDTA) as scavengers, respectively. From Fig. 7, %OH and h^+ are both active species in the degradation process, and %OH is the main active species for the degradation of 4-NP and CIP, whereas h^+ is the main active species for the degradation of DEP. In addition, photogenerated electrons also have an effect on the degradation of 4-NP, whereas the degradation of DEP and CIP are hardly affected by electrons. The results show that some photogenerated electrons were consumed in the degradation of 4-NP, while the photodegradation of CIP and DEP does not need electrons. The results also clearly explain why the photocatalytic rate of hydrogen evolution in a solution of 4-NP is smaller than that in the CIP and DEP solution.

Furthermore, according to DFT, the HOMO and LUMO of organic pollutants were calculated to investigate the different photodegradation rates of 4-NP, CIP, and DEP over GQDs/TCN-0.4 in the photocatalytic system. As shown in Fig. 8, the highest degradation rate of 4-NP over the GQDs/TCN-0.4 catalyst could be mainly due to the smaller molecule 4-NP than that of CIP and DEP, leading to more stability of CIP and DEP than 4-NP. The overlapping of electron clouds in the LUMO and HOMO of DEP would accelerate the recombination of e^- and h^+ in these organic molecules, whereas the electron clouds in the LUMO and HOMO of CIP are partially separated [17], resulting in better separation of electrons and holes. The result explains why the photodegradation

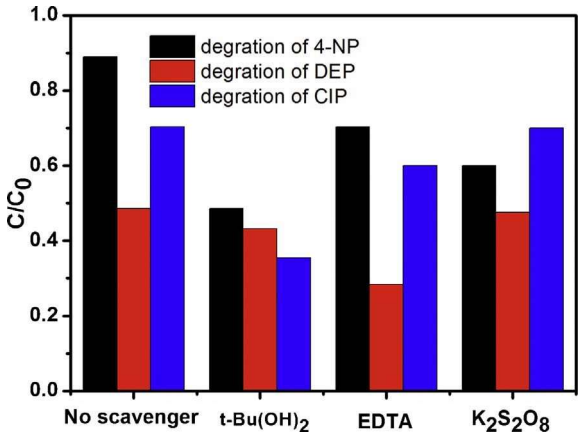

Fig. 7. Removal rate of 4-NP, DEP and CIP over the 5%GQDs/TCN-0.4 after the addition of different scavengers for 2 h reaction.

rate of CIP is better than DEP over GQDs/TCN-0.4, consistent with the above experimental results of catalytic degradation.

As shown in Fig. S9 in SI, the Mott-Schottky (MS) plots of Mn-NTiO_2 and CNS show that the potentials of the conduction bands are −0.54 V and −0.6 V for Mn-N-TiO_2 and CNS, respectively. Combined with the optical absorption edge of Mn-N-TiO_2 and CNS, the E_{VB} of MnN-TiO_2 and CNS are calculated as 2.36 V and 2.2 V ($E_{CB} = E_{VB} - E_g$), respectively. Therefore, h^+ on the VB of CNS can react with OH^- to produce %OH because the oxidation potentials of VB of CNS is larger than that of %OH/OH^- (1.99 V vs. NHE). The VB of Mn-N-TiO_2 is more positive than the standard redox potential E^0(%OH/H_2O) (2.27 V vs. NHE) under alkaline conditions so that H_2O can be directly oxidized by holes to form %OH [51].

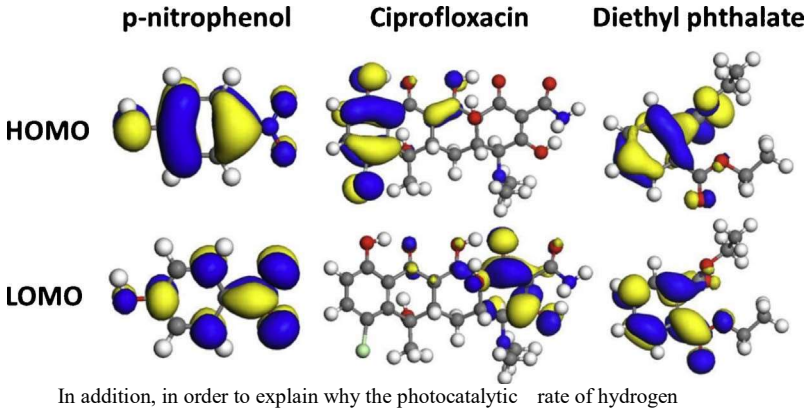

Fig. 8. Frontier electron densities of LUMO and HOMO of 4-NP, CIP and DEP.

In addition, in order to explain why the photocatalytic rate of hydrogen production is different in the presence of different organic pollutants, LC-MS tests were also investigated. The generated intermediates and final products were detected by HPLC−MS, and the 4-NP and DEP degradation pathways were studied. As shown in Fig. S10, the 4-NP characteristic ion peak corresponds to the MS fragmentation pattern at m/z = 138. With an increase of photocatalytic time, the characteristic pattern at m/z = 138 significantly decreases, and some mass peaks at m/z 103, 108, 116, 128 and 144 are found in the spectra, suggesting the occurrence of hydroxylation and demethylation reactions of 4-NP molecules. Based on the above photocatalytic experiments, under the attack of holes or e^-, these intermediates are further mineralized to CO_2 and H_2O. According to the above analyses, the possible degradation scheme of 4-NP was proposed in Fig. 9a. For the first path of 4-NP degradation, the hydroxyl group (eOH) favors the electrophilic attack of %OH on the ortho- and para- positions along with a fracture of hydrogen bonds in the benzene ring. And then it generates hydroquinone that is capable of being rapidly oxidized to benzoquinone and catechol (or hydroquinol) identified by the patterns at m/z 108 and 110, respectively [52]. During the transformation between hydroquinone and catechol, electrons would be consumed, leading to a decrease of photocatalytic efficiency of hydrogen production. The %OH radicals further attack the aromatic ring to generate some intermediates (m/z = 110, 118 and 144), and ultimately are mineralized to CO_2 and H_2O [52,53]. For the second path of 4-NP degradation, a successive electrophilic attack of %OH on hydroquinone forms hydroxyquinol (m/ z = 128). And the hydroxyquinol would be transformed into 5-hydroxycyclohex-2-ene-1,4-dione (m/z = 116) after accepting electrons. Then the intermediates ring-open to generate carboxylic acids such as fumaric acid and oxalic acids (m/z = 118 and 103), and finally are mineralized to CO_2 and H_2O attacked by %OH [52]. Combined with Fig. S10, the second path may be the major one for 4-NP degradation. This result confirms that e^- competition would occur between the 4-NP photodegradation and photocatalytic production of H_2. Accordingly, the photogenerated electrons are not all used for photocatalytic hydrogen production, resulting in a decrease of photocatalytic efficiency of hydrogen production.

Different from 4-NP, the degradation of DEP does not consume photogenerated electrons. As shown in Fig. 9b and Fig. S11, DEP shows a base peak corresponding to sodium adducts $[M+Na]^+$ at 245 m/z [54]. Under the attack of holes, the aromatic ring would open to generate some intermediates (m/z = 223, 177 and 182), and ultimately be mineralized to CO_2 and H_2O [55,56]. No intermediate products consume any electrons in the degradation process of DEP, which does not affect the photocatalytic H_2 evolution. The above results demonstrate the photocatalytic rate of H_2 evolution in the DEP solution is much higher than that in the 4-NP solution, in consistent with the photocatalytic experimental results.

Based on the above results and discussion, a possible mechanism is

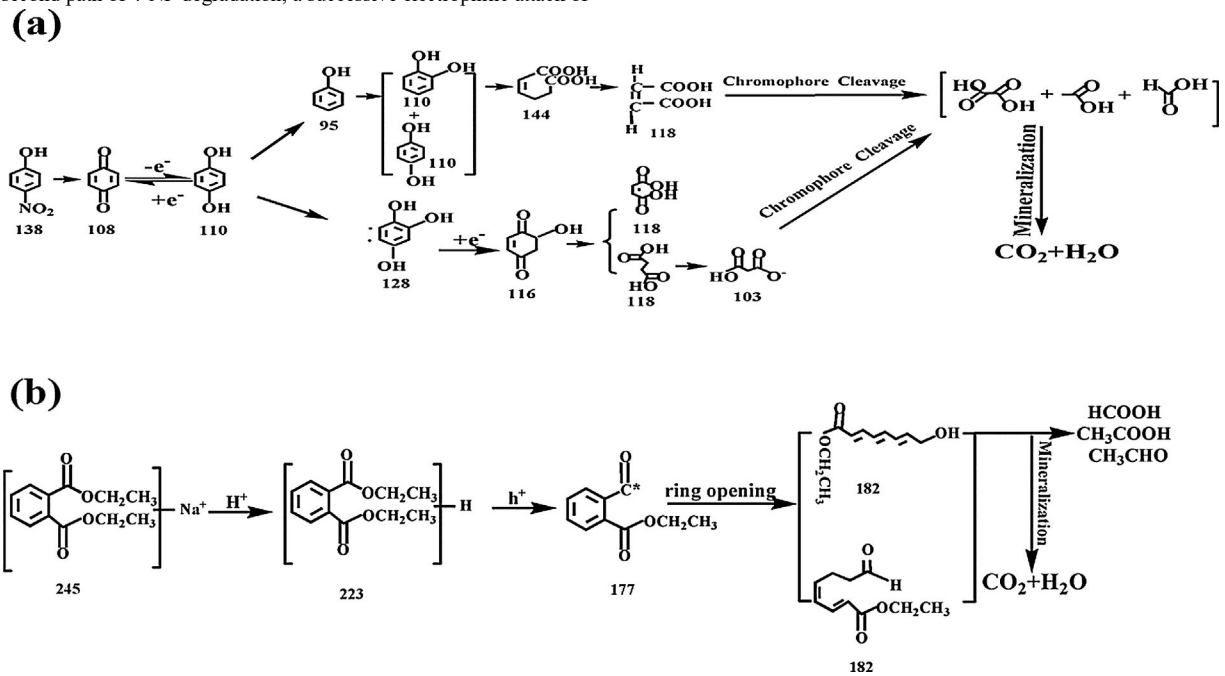

Fig. 9. Proposed reaction mechanisms of the degradation of 4-NP (a) and DEP (b) by the 5%GQDs/TCN-0.4.

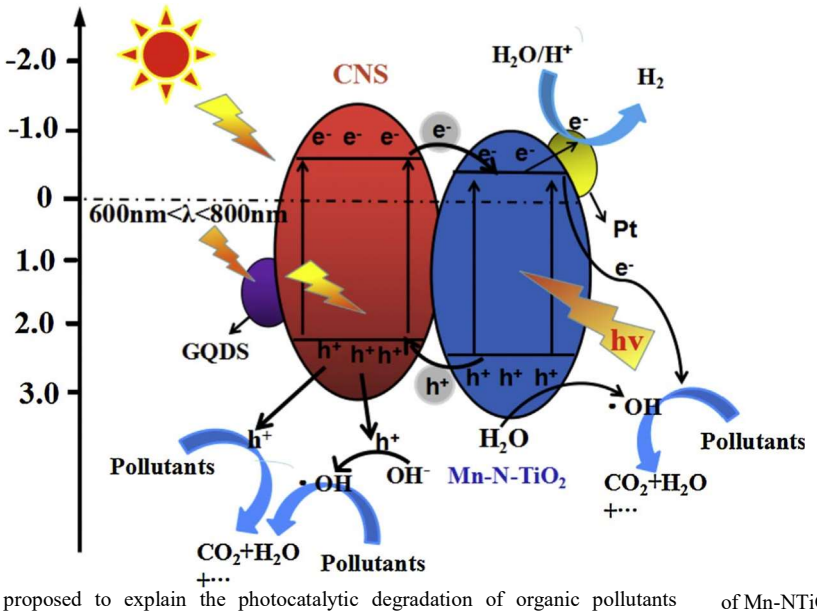

proposed to explain the photocatalytic degradation of organic pollutants coupled with simultaneous photocatalytic H_2 evolution over the GQDs/TCN-0.4. As shown in Scheme 1, when the GQDs/TCN-0.4 catalyst is irradiated under simulated solar radiation, GQDs can absorb long wavelengths of light (600–800 nm) and then emit short wavelength light (λ < 500 nm) that is absorbed by Mn-N-TiO_2 and CNS to generate electrons (e^-) and holes (h^+). CNS and Mn-N-TiO_2 can simultaneously absorb light to generate electrons and holes, and the electrons are excited from the VB to CB. The electrons on the CB of CNS transfer to the CB of Mn-N-TiO_2, and then react with water on the surface of GQDs or Pt to form H_2. During the photodegradation of 4-NP, a small amount of electrons would be consumed by the intermediates of 4-NP, so that the photocatalytic rate of H_2 evolution in the 4-NP solution is smaller than that in solutions of CIP or DEP. Accordingly, the holes on the VB of Mn-N-TiO_2 transfer to the VB of CNS, and then gradually decompose 4-NP, CIP or DEP to CO_2 and H_2O. And these organic pollutants are also mineralized via %OH generated from OH^- oxidation by holes. The mechanism explains the multiple effects of GQDs in the GQDs/TCN-0.4 composite and supports the photocatalytic photodegradation of organic pollutants coupled with simultaneous photocatalytic H_2 evolution over GQDs/TCN-0.4. The mechanism clearly shows the different effect of organic pollutants on photocatalytic H_2 evolution.

4. Conclusions

In summary, GQDs/TCN composite catalysts have been successfully prepared by combining GQDs and g-C_3N_4 nanosheets with Mn-N-TiO_2 for the first time. Systematic characterizations were done for GQDs/ TCN to confirm this heterostructured composite. The experimental results show that the 5%GQDs/TCN-0.4 catalyst has the best photocatalytic hydrogen production and organic pollutant degradation rate under simulated solar irradiation in the simultaneous photocatalytic oxidation and reduction system. The photocatalytic rates of H_2 evolution in the solutions of 4-NP, CIP and DEP are all larger than that in pure water system over the 5%GQDs/TCN-0.4, whereas the H_2 evolution rate in the solution of 4-NP is smaller than that in the solutions of CIP and DEP. Accordingly, the photodegradation rate of 4-NP is larger than that of CIP and DEP. For the first time, the present work clarifies the effect of different organic pollutants on the photocatalytic rate of H_2 evolution, as well as different photodegradation rates of 4-NP, CIP, and DEP over the same composite catalyst via DFT and LC-MS. A photocatalytic mechanism was proposed to explain the photocatalytic enhancement of the GQDs/TCN-0.4 catalyst and the effect of different organic pollutants on the photocatalytic H_2 evolution.

Scheme 1. Possible photocatalytic mechanism of degradation of organic pollutants coupled with simultaneous photocatalytic H_2 evolution over GQDs/TCN-0.4 under simulated solar irradiation.

Acknowledgements

We gratefully acknowledge the financial support of the NSF of China (51622806, 51378246, 51238002, and 51272099) and the NSF of Jiangxi Province (20162BCB22017, 20165BCB18008, 20171ACB20017, 20133ACB21001, and 20122BCB23013). SLS acknowledges the support of the US Department of Energy, Office of Basic Energy Sciences, Division of Chemical, Biological and Geological Sciences under grant DE-FG02-86ER13622.A000.

Appendix A. Supplementary data

Electronic Supplementary Information available: the picture of photocatalytic reactor system; SEM, EDS spectra, DRS spectra, absorption spectra, Mott-Schottky plots, specific surface area, pore volume and pore size of the as-prepared catalysts; enlarged profile of Mn-NTiO2 of the (101) XRD peak; the characteristic peak of Raman spectra of as-prepared catalysts; HPLC spectra of the catalytic degradation of DEP and CIP, as well as EIS spectra of 4-NP and DEP over the GQDs/TCN-0.4 under simulated solar irradiation. These supplementary materials can be found in the online version at http://www.sciencedirect.com.

References

[1] L. Wollenberger, B. Halling-Sørensen, K.O. Kusk, Chemosphere 40 (2000) 723–730. [2] J.L. Martinez, Environ. Pollut. 157 (2009) 2893–2902.
[3] M.X. Jia, J.X.J. Xia. Di, Y.L. Liu, R. Chen, Z.G. Chen, S. Yin, H.M. Lia, Chem. Eng. J. 331 (2018) 355–363.
[4] H.J. Gan, Z. Wang, H.M. Li, Y.R. Wang, L.P. Sun, Y.F. Li, RSC. Adv. 6 (2016) 5192–5197.
[5] J.J. Fang, W. Wang, C. Zhu, L. Fang, J.Y. Jin, Y.R. Ni, C.H. Lu, Z.Z. Xu, Appl. Catal. B: Environ. 217 (2017) 100–107.
[6] M. Eisenstein, Nature 521 (2015) S52–S55.
[7] Z.J. Niu, Y.J. Wang, H. Lin, F.Y. Jin, Y. Li, J.F. Niu, Chem. Eng. J. 328 (2017) 228–235.
[8] A. Kubacka, M. Fernandez-Garcia, G. Colon, Chem. Rev. 112 (2012) 1555–1614.
[9] X.B. Chen, S.H. Shen, L.J. Guo, S.S. Mao, Chem. Rev. 110 (2010) 6503–6570.
[10] N. Zhang, M.Q. Yang, S.Q. Liu, Y.G. Sun, Y.J. Xu, Chem. Rev. 115 (2015) 10307–10377.
[11] Y. Ma, X.L. Wang, Y.S. Jia, X.B. Chen, H.X. Han, C. Li, Chem. Rev. 114 (2014) 9987–10043.
[12] Q. Wang, Y.L. Jia, M.P. Wang, W.H. Qi, Y. Pang, X.M. Cui, W.H. Ji, J. Yi, J. Phys. Chem. C 119 (2015) 22066–22071.
[13] W. Zhou, W. Li, J.Q. Wang, Y. Qu, Y. Yang, Y. Xie, K.F. Zhang, L. Wang, H.G. Fu, D.Y. Zhao, J. Am. Chem. Soc. 136 (2014) 9280–9283.
[14] W.H. Dong, D.D. Wu, M.J. Luo, Q.J. Xing, H. Liu, J.P. Zou, X.B. Luo, X.B. Min, H.L. Liu, S.L. Luo, C.T. Au, J. Catal. 349 (2017) 218–225.
[15] J.P. Zou, D.D. Wu, J.M. Luo, Q.J. Xing, X.B. Luo, W.H. Dong, S.L. Luo, H.M. Du, S.L. Suib, ACS Catal. 6 (2016) 6861–6867.
[16] K.X. Li, Z. Zeng, L.S. Yan, M.X. Huo, Y.H. Guo, S.L. Luo, X.B. Luo, Appl. Catal. B: Environ. 187 (2016) 269–280.
[17] S.Q. Zhang, L.L. Wang, C.B. Liu, J.M. Luo, J. Crittenden, X. Liu, T. Cai, J.L. Yuan, Y. Pei, Y.T. Liu, Water Res. 121 (2017) 11–19.
[18] K.H. Chu, L.Q. Ye, W. Wang, D. Wu, D.K.L. Chan, C.P. Zeng, H.Y. Yip, J.C. Yu, P.K. Wong, Chemosphere 183 (2017) 219–228.
[19] Z.F. Jiang, W.M. Wan, W. Wei, K.M. Chen, H.M. Li, P.K. Wong, J.M. Xie, Appl. Catal. B: Environ. 204 (2017) 283–295.
[20] R. Asahi, T. Morikawa, T. Ohwaki, K. Aoki, Y. Taga, Science 293 (2001) 269–271.
[21] W.Y. Choi, A. Termin, M.R. Hoffmann, J. Phys. Chem. 98 (1994) 13669–13679.
[22] I.K. Konstantinou, T.A. Albanis, Appl. Catal. B: Environ. 49 (2004) 1–14.
[23] U.I. Gaya, A.H. Abdullah, J. Photochem. Photobiol. C 9 (2008) 1–12.
[24] P.S. Yan, Z.R. Xin, M. Hui, D.D. Li, P.X. Jun, Q. Fei, C. Wei, Appl. Catal. B: Environ. 218 (2017) 208–219.
[25] F.C. Peng, H.L. Gao, G.L. Zhang, Z.Q. Zhu, J. Zhang, Q.J. Liu, Material 10 (2017) 209.
[26] J.J. Lia, S.C. Cai, Z. Xu, X. Chen, H.P. Jia, J. Chen, J. Hazard. Mater. 325 (2017) 261–270.

[27] Y. Chen, K.R. Liu, J. Alloys Compd. 697 (2017) 161–173.
[28] J.W. Liu, R. Han, Y. Zhao, H.T. Wang, W.J. Lu, T.F. Yu, Y.X. Zhang, J. Phys. Chem. C 115 (2011) 4507–4515.
[29] L. Feng, H. Jiang, M.M. Zou, F.Q. Xiong, A.S. Ganeshraja, E. Pervaiz, Y.A. Liu, S.Y. Zou, M.H. Yang, J. Nano Res. 18 (2016) 278.
[30] F. Dong, H.Q. Wang, Z.B. Wu, J. Phys. Chem. C 38 (2009) 16717–16723.
[31] A. Petala, Z. Frontistis, M. Antonopoulou, I. Konstantinou, D.I. Kondarides, D. Mantzavinos, Water Res. 81 (2015) 157–166.
[32] C. Wang, M.H. Cao, P.F. Wang, Y.H. Ao, J. Hou, J. Qian, Appl. Catal. A. Gen. 473 (2014) 83–89.
[33] A. Petala, D. Tsikritzis, M. Kollia, S. Ladas, S. Kennou, D.I. Kondarides, Appl. Surf. Sci. 305 (2014) 281–291.
[34] M.H. Cao, P.F. Wang, Y.H. Ao, C. Wang, J. Hou, J. Qian, Chem. Eng. J. 264 (2015) 113–124.
[35] Z. Wu, R. Jin, H. Wang, Y. Liu, Catal. Commun. 6 (2009) 935–939.
[36] X.C. Wang, K. Maeda, A. Thomas, K. Takanabe, G. Xin, J.M. Carlsson, K. Domen, M. Antonietti, Nat. Mater. 8 (2009) 76–80.
[37] Z.W. Zhao, Y.J. Sun, F. Dong, Nano 7 (2015) 15–37.
[38] G.G. Zhang, Z.A. Lan, L.H. Lin, S. Lin, X.C. Wang, Chem. Sci. 7 (2016) 3062–3066.
[39] Y.F. Li, R.X. Jin, Y. Xing, J.Q. Li, S.Y. Song, X.C. Liu, M. Li, R.C. Jin, J. Mater. Chem.
6 (2016) 1601273.
[40] X.H. Pang, Y. Zhang, C. Liu, Y. Huang, Y.G. Wang, J.H. Pan, Q. Wei, B. Dua, J. Mater. Chem. B. 4 (2016) 4612–4619.
[41] D.L. Jiang, Y. Zhang, H.Y. Chu, J. Liu, J. Wan, M. Chen, RSC Adv. 4 (2014) 16163–16171.
[42] K. Fukui, Science 218 (1982) 747–754.
[43] J.J. Yao, M.R. Hoffmann, N.Y. Gao, Z. Zhang, L. Li, Water Res. 45 (2011) 5886–5894.
[44] A.P. Larios, A.H. Gordillo, G.M. Mendoza, L.L. Rojas, Á. Mantill, R. Gómez, Catal. Today 266 (2016) 9–16.
[45] Z. Luo, A.S. Poyraz, C.H. Kuo, R. Miao, Y.T. Meng, S.Y. Chen, T. Jiang, C. Wenos, S.L. Suib, Chem. Mater. 27 (2015) 6–17.
[46] D. Qu, M. Zheng, P. Du, Y. Zhou, L.G. Zhang, D. Li, H.Q. Tan, Z. Zhao, Z.G. Xie, Z.C. Sun, Nano 5 (2013) 12272–12277.
[47] Z. Wei, F.F. Liang, Y.F. Liu, W.J. Luo, J. Wang, W.Q. Yao, Y.F. Zhu, Appl. Catal. B: Environ. 201 (2017) 600–606.
[48] J.H. Shen, Y.H. Zhu, X.L. Yang, C.Z. Li, Chem. Commun. 48 (2012) 3686–3699.
[49] Q. Liang, Z. Li, X. Yu, Z.H. Huang, F. Kang, Q.H. Yang, Adv. Mater. 27 (2015) 4634–4639.
[50] J. Peng, W. Gao, B.K. Gupta, Z. Liu, R.R. Aburto, L.H. Ge, L. Song, L.B. Alemany, X.B. Zhan, G.H. Gao, S.A. Vithayathil, B.A. Kaipparettu, A.A. Marti, T. Hayashi, J.J. Zhu, P.M. Ajayan, Nano. Lett. 12 (2012) 844–849.
[51] L. Wu, J.C. Yu, X.Z. Fu, J. Mol. Catal. A: Chem. 244 (2006) 25–32.
[52] A.D. Paola, V. Augugliaro, L. Palmisano, G. Pantaleo, E. Savinov, J. Photochem. Photobiol. A 155 (2003) 207–214.
[53] M.H. Zhou, L.C. Lei, Chemosphere 63 (2006) 1032–1040.
[54] Y.W. Ma, Y. Hashi, F. Ji, J.M. Lin, J. Sep. Sci. 33 (2010) 251–257.
[55] Y.H. Chen, L.L. Chen, N.C. Shang, J. Hazard. Mater. 172 (2009) 20–29.
[56] S. Kaneco, H. Katsumata, T. Suzuki, K. Ohta, Chem. Eng. J. 125 (2006) 59–66.